Three-Dimensional Electron Realm in VSe₂ by Soft-X-Ray Photoelectron Spectroscopy: Origin of Charge-Density Waves

Vladimir N. Strocov,[1,*] Ming Shi,[1] Masaki Kobayashi,[1] Claude Monney,[1] Xiaoqiang Wang,[1] Juraj Krempasky,[1]
Thorsten Schmitt,[1] Luc Patthey,[1] Helmuth Berger,[2] and Peter Blaha[3]

[1]*Swiss Light Source, Paul Scherrer Institute, CH-5232 Villigen-PSI, Switzerland*
[2]*Institut de Physique de la Matière Complexe, EPFL, CH-1015 Lausanne, Switzerland*
[3]*Institut für Materialchemie, Technische Universität Wien, A-1060 Wien, Austria*

The resolution of angle-resolved photoelectron spectroscopy (ARPES) in three-dimensional (3D) momentum **k** is fundamentally limited by ill defined surface-perpendicular wave vector $k_\perp$ associated with the finite photoelectron mean free path. Pushing ARPES into the soft-x-ray energy region sharpens the $k_\perp$ definition, allowing accurate electronic structure investigations in 3D materials. We apply soft-x-ray ARPES to explore the 3D electron realm in a paradigm transition metal dichalcogenide VSe₂. Essential to break through the dramatic loss of the valence band photoexcitation cross section at soft-x-ray energies is the advanced photon flux performance of our synchrotron instrumentation. By virtue of the sharp 3D momentum definition, the soft-x-ray ARPES experimental band structure and Fermi surface of VSe₂ show a textbook clarity. We identify pronounced 3D warping of the Fermi surface and show that its concomitant nesting acts as the precursor for the exotic 3D charge-density waves in VSe₂. Our results demonstrate the immense potential of soft-x-ray ARPES to explore details of 3D electronic structure.

Introduction.—Electronic structure of crystalline materials is their fundamental characteristic, which is the basis of almost all their physical and chemical properties. Angle-resolved photoemission spectroscopy (ARPES) is the main experimental tool to study all electronic structure aspects with resolution in electron momentum [1]. This ability is based on the fact that the photon promoted electron excitation in the crystal bulk, from an initial state in the valence band to final state in the unoccupied states continuum, conserves the three-dimensional (3D) momentum **k**. However, resolving its surface-perpendicular $k_\perp$ component required for 3D materials faces two fundamental difficulties: (1) Whereas the surface-parallel component $\mathbf{k}_\parallel$ is conserved at the photoelectron escape stage and can be directly measured in the experiment, $k_\perp$ is distorted by the momentum absorbed by the surface barrier. It can only be recovered if one knows the $E(k_\perp)$ dispersion of the final state back at the photoexcitation stage where the full 3D momentum was conserved. The free-electron (FE) approximation commonly used at this point has only a limited applicability, because for many materials the final states can feature complicated non-FE and excited-state self-energy effects [2,3]; (2) the final state confinement within the photoelectron escape depth λ results, by the Heisenberg uncertainty principle, in intrinsic broadening of $k_\perp$ defined by $\Delta k_\perp = \lambda^{-1}$. The valence band $E(k_\perp)$ appearing in the measured spectrum is then an average over the $\Delta k_\perp$ interval, which intrinsically limits resolution of the ARPES experiment in $k_\perp$ [4].

Pushing ARPES from the conventional vacuum ultraviolet (VUV) to soft-x-ray photon energy range around

1 keV [5–7] addresses both problems: (1) The photoelectron energies become much larger than the crystal potential modulations, which makes the final states truly FE-like; (2) the increase of λ with energy following the "universal curve" [8] results in sharpening of the $\Delta k_\perp$ intrinsic accuracy. Further advantages of soft-x-ray ARPES (SX-ARPES) include larger bulk sensitivity and simplified matrix elements. However, SX-ARPES notoriously suffers from a loss of photoexcitation cross section of valence states by a few orders of magnitude compared to the VUV energy range. Here, we have broken through this problem by using the high-resolution soft-x-ray beamline ADRESS (Advanced Resonant Spectroscopies) [9] at Swiss Light Source (SLS) delivering particularly high photon flux.

Here, we apply SX-ARPES to explore 3D electronic structure of a typical layered transition metal dichalcogenide (TMDC) material VSe₂. A wide van der Waals gaps between the chalcogen-metal-chalcogen trilayers result in its quasi-2D properties [10,11]. The states derived from the out-of-plane orbitals like Se $4p_z$ retain nevertheless a 3D character with their $k_\perp$ dispersion range of a few eV. In VUV-ARPES, their response is distorted by non-FE final states and $\Delta k_\perp$ broadening comparable with the Brillouin zone (BZ) height $k_\perp^{BZ}$ [2,3].

Typical of the TMDCs are charge-density waves (CDWs) appearing due to an interplay of the electron and phonon subsystems in the crystal [12–14]. They may form, in particular, when large areas of the Fermi surface (FS) exhibit nesting with a **q**-vector vector leading to a soft phonon mode at this **q** freezing into the CDW. VSe₂ shows a CDW transition at $T_C \sim 110$ K accompanied

by characteristic anomalies in transport and magnetic properties. Intriguingly, in contrast to most of the TMDCs [10,13,15], the CDWs in VSe2 are 3D in the sense of their wave vector $\mathbf{q}^{\text{CDW}}$ having a large out-of-plane component [10,16]. The question is, are there precursors of such exotic 3D CDWs in nesting properties of the FS?

Methods.—Single crystals of VSe2 were grown by the chemical vapor transport method. The in-plane and out-of-plane lattice constants are 3.346 and 6.096 Å, respectively. For the ARPES measurements the samples were *in situ* cleaved. The experiments were performed at the ADRESS beamline [9] of SLS. This beamline delivers soft-x-ray radiation with variable linear and circular polarizations in the energy range from 300 to 1600 eV. Its key feature is high photon flux up to 10^{13} (photons/s)0.01%BW at 1 keV. The ARPES end station uses a vertical scattering plane geometry (see the supplemental material [17]). The manipulator CARVING provides us with 3 angular degrees of freedom. The sample environment allows cooling down to 10.7 K. The photoelectron analyzer PHOIBOS-150 usually operated with an acceptance of $\pm 6°$ sufficient to cover more than one BZ. In the present experiment, the analyzer slit was perpendicular to the scattering plane. We used p polarization of incident light which delivered stronger intensity compared to s polarization.

The band structure computations were performed within the standard density functional theory (DFT) formalism with the generalized gradient approximation for the electron exchange correlation. We employed the full-potential (linearized) augmented plane waves + local orbitals method implemented in the WIEN2K package [18].

Band structure.—We start with a general picture of the 3D electronic structure of VSe2. In the ARPES experiment, one navigates in the 3D $\mathbf{k}$ space by varying $\mathbf{k}_{\parallel}$ through the emission angle ϑ, and varying $k_{\perp}$ through photon energy $h\nu$ (with corrections for the photon momentum $p^{\text{ph}} = h\nu/c$) [19,20]. From extremal behavior of the ARPES spectra with $h\nu$, we found $k_{\perp}$ to pass the Γ point at 885 eV; see the BZ sketch in Fig. 1(a). The corresponding ARPES intensity image $I(E, k_{\parallel})$ along the $M'\Gamma M$ line is shown in Fig. 1(b). The energy resolution ΔE was here ~ 120 meV and acquisition time only 7 min. The $I(E, k_{\perp})$ map along the surface-perpendicular ΓA direction in Fig. 1(c) was generated from images measured under $h\nu$ variation, with $h\nu$ rendered into $k_{\perp}$ assuming FE final states with an empirical inner potential of 7.5 eV. The experimental dispersions agree with the previous VUV-ARPES study [2] where control over $k_{\perp}$ was achieved by determination of the final states by very-low-energy electron diffraction. Figures 1(d) and 1(e) zoom in the Fermi level E_F region along the $M'\Gamma M$ and $K\Gamma K$ lines, respectively. ΔE was sharpened here to ~ 70 meV and acquisition time increased to 40 min.

Statistics of our data is remarkable because at energies around 900 eV the V 3d and Se 4p cross sections drop by a
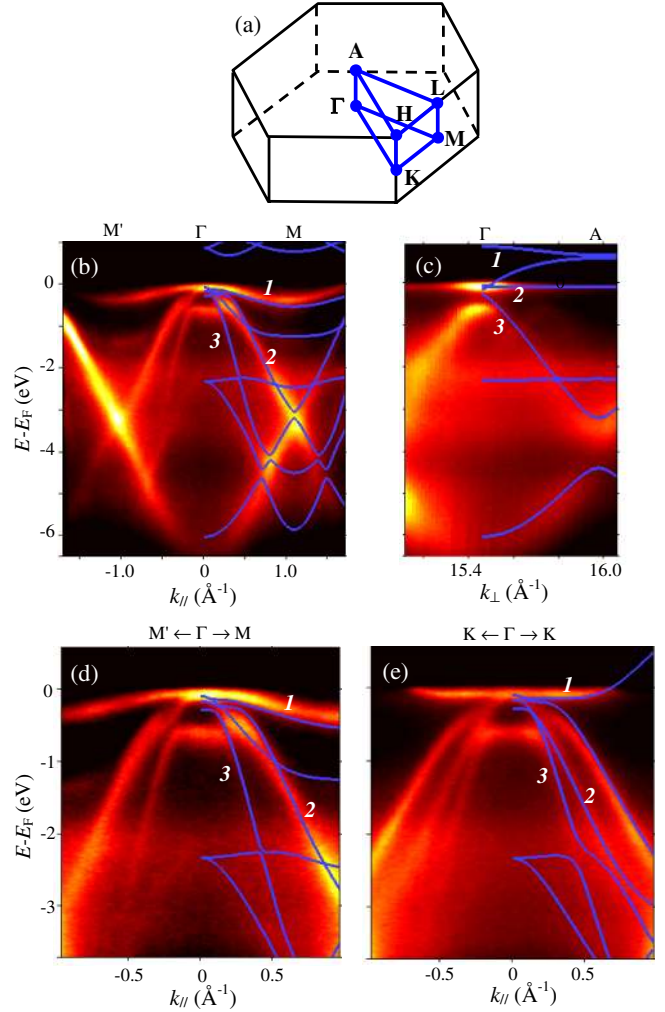

FIG. 1 (color online).   SX-ARPES experimental band structure of VSe2 along selected BZ lines. (a) BZ sketch; (b–e), experimental ARPES intensity in color scale: (b) $I(E, k_{\parallel})$ image along the $M'\Gamma M$ line ($h\nu = 885$ eV to deliver $k_{\perp} = 0$); (c) $I(E, k_{\perp})$ map along the ΓA line ($h\nu$ variation from 845 to 960 eV; note different $k_{\perp}$ scale). To compensate the cross section variations, the individual $h\nu = $ const slices are normalized in integral intensity; (d–e) high-resolution $I(E, k_{\parallel})$ images along the $M'\Gamma M$ and $K\Gamma K$ lines ($h\nu = 885$ eV). The V 3d band (marked 1) forms the FS, and the Se $4p_{xy}^*$ (2) and $4p_z^*$ (3) are deeper in the valence band. The DFT band calculations (blue lines) remarkably agree with the experiment except underestimation of the Se $4p_z^* - p_{xy}^*$ hybridization near the Γ point.

factor of ~ 1800 and 34, respectively, compared to a typical VUV-ARPES photon energy of 50 eV [21]. Profound contrast and dispersion of the spectral structures makes redundant any image enhancement like subtraction of angle-integrated background [22] or second-derivative representation [23]. This is remarkable because in the soft-x-ray range the photoelectron wavelength is comparable with amplitudes of the thermal motion of atoms, which acts to destroy the coherent spectral structures through their Debye-Waller amplitude reduction, broadening and piling

up an incoherent **k**-integrated background [20,24]. Working at temperatures around 11 K, we minimized these destructive effects even for VSe$_2$ having rather low Debye temperature of 220 K [25]. Furthermore, excellent agreement of our DFT calculations (blue lines in Fig. 1) with the experiment demonstrates a weakly correlated nature of VSe$_2$. The calculations are seen however to underestimate the hybridization between the Se $4p_z^*$ and $4p_{xy}^*$ bands near the Γ point.

Fermi surface.—Accurate control over $k_\perp$ in our experiment has allowed us to slice the FS in different planes. Figure 2(b) shows the ΓALM slice acquired under $h\nu$ variation. Because of high kinetic energies, the iso-$h\nu$ trajectories (dashed lines) show only small $k_\perp$ variations with $\mathbf{k}_\parallel$. Figures 2(c) and 2(e) display the ΓKM ($k_\perp = 0$) and AHL ($k_\perp = \Gamma A$) slices, respectively, and Fig. 2(d) a slice between them at $k_\perp \sim k_\perp^{BZ}/2$ acquired under a variation of ϑ. The ΓKM and ALH maps follow the sixfold symmetry characteristic of these symmetry planes, and the map between them displays asymmetric dogbone electron pockets following the threefold symmetry of the BZ interior. The definition of our experimental FS is much superior to previous VUV-ARPES results [23], which showed elliptical FS pockets from the AHL plane mixed with streaks near $\mathbf{k}_\parallel = 0$ from the ΓKM plane.

Topology of the FS expected from our DFT calculations is shown in Fig. 2(a), and its contours in the above BZ planes superimposed on the experimental data (blue lines). Again, the calculations show remarkable agreement with the experiment. For the ΓALM plane, the experimental FS exhibits somewhat larger area than the calculation suggesting a stronger out-of-plane conductivity. For the AHL slice, even fine details are reproduced such as a tiny rectangular distortion of the FS pockets around the L points. For the ΓKM slice, the straight sections of the FS are well reproduced. The intense spot at the Γ point comes

from the intensity rise in the $4p_{xy}^*$ band just below E_F, see Fig. 1(b), and streaks going from Γ in the K direction follow the V $3d$ band staying there flat near E_F; see Fig. 1(e). We note no signs of the CDW superstructure in our data, indicating that the CDW induced perturbation of the crystal potential is weak enough to leave the spectral weight follow the fundamental periodicity of the VSe$_2$ lattice [26].

Origin of charge-density waves.—With confidence of our accurate navigation in 3D **k** space, we turned to investigation of the electronic structure precursors of the 3D CDWs in VSe$_2$. Theoretically, interaction of the electron and phonon systems in the crystal forms a CDW with wave vector **q** under the instability condition [14]

$$\frac{4\bar{\eta}_{\mathbf{q}}^2}{\hbar\omega_{\mathbf{q}}} \geq \frac{1}{\chi_{\mathbf{q}}} + 2\bar{U}_{\mathbf{q}} - \bar{V}_{\mathbf{q}},$$

where $\bar{\eta}_{\mathbf{q}}$ is the electron-phonon interaction corresponding to a phonon mode of energy $\omega_{\mathbf{q}}$, $\chi_{\mathbf{q}}$ is the (real part of) electronic susceptibility at the static $\omega \to 0$ limit, and $\bar{U}_q$ and $\bar{V}_q$ are matrix elements of their Coulomb and exchange interactions, respectively. This inequality to set up CDWs is driven either by increase of the left-hand "phononic" side due to strong electron-phonon interaction and availability of soft phonon modes [13,27], or by decrease on the right-hand "electronic" side due to singularity of $\chi_{\mathbf{q}}$ due to response of the conduction electrons coupled by the corresponding soft phonon mode. The latter scenario usually takes place when large parallel areas of the FS nest at certain **q** resulting in a peak of $\chi_{\mathbf{q}}$ [10,13,15]. In contrast to the one-dimensional (1D) case automatically leading to the paradigm Peierls transition, realization of this scenario in 3D is most restrictive because the nesting areas should match their curvatures in all three dimensions. We will illustrate how this is nevertheless realized in VSe$_2$.
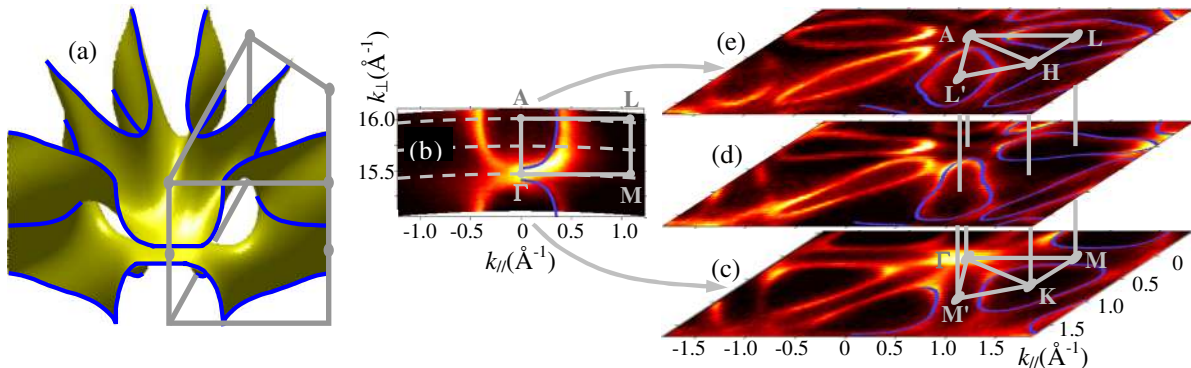

FIG. 2 (color online).   Experimental FS slices in selected BZ planes. (a) DFT calculated FS of VSe$_2$ with its contours in the symmetry planes (blue lines); (b) experimental FS slice in the ΓALM plane of the BZ ($h\nu = 845$ to 960 eV). Dashed lines are iso-$h\nu$ trajectories; (c–e) experimental FS slices in the ΓKM central plane ($h\nu = 885$ eV), a plane at half the BZ heights (915 eV) and ALH face plane (945 eV), respectively. No image enhancement or symmetrization has been applied to these maps. By virtue of well-defined $k_\perp$ the experimental FS demonstrates a textbook clarity. The DFT calculations (blue lines) agree with the experiment, except for the central spot and streaks in the ΓKM plane coming from the V $3d$ and Se $4p_{xy}^*$ bands in vicinity of E_F.

The 3D CDWs are characterized by their $\mathbf{q}^{\mathrm{CDW}} = q_{\parallel}^{\mathrm{CDW}}\mathbf{a}^* + q_{\perp}^{\mathrm{CDW}}\mathbf{c}^*$, where $\mathbf{a}^*$ and $\mathbf{c}^*$ are the in-plane and out-of-plane reciprocal lattice unit vectors, respectively. The actual $q_{\parallel}^{\mathrm{CDW}}$ and $q_{\perp}^{\mathrm{CDW}}$ in VSe$_2$ determined by x-ray diffraction are around the 1/4- and 1/3-commensurate values 0.54 Å^{-1} and 0.34 Å^{-1}, respectively, with some scatter in the literature regarding their exact values, commensurability and transition temperatures [16,28]. VUV-ARPES studies of VSe$_2$ have related the $q_{\parallel}^{\mathrm{CDW}}$ component to nesting of the FS along the $\mathbf{a}^*$ axis [23,29] and even identified a weak spectral weight reduction in the corresponding $\mathbf{k}_{\parallel}$ regions [23]. According to theoretical analysis [10], the $q_{\perp}^{\mathrm{CDW}}$ one would originate from nesting along the $\mathbf{c}^*$ axis owing to warping of the FS in the $k_{\perp}$ direction. However, VUV-ARPES failed to yield any unambiguous evidence of this [30] because of ill defined low-energy final states.

To resolve the origin of $q_{\perp}^{\mathrm{CDW}}$, we have measured the out-of-plane FS cut in the $MLL'M'$ plane; Fig. 3(a). This plane goes through the region of (flattened by the rectangular distortion) FS areas which nest with $q_{\parallel}^{\mathrm{CDW}}$; see Fig. 2(c). One of the $I(E, k_{\parallel})$ images, measured near the MM' line at $k_{\perp} = 0$, is shown in Fig. 3(b). The experimental FS cut obtained under $h\nu$ variations is shown in Fig. 3(c). The cut shows 3D warping with concave and convex regions, which clearly nest through the 3D $\mathbf{q}$ vector (arrows) closely matching that of the 3D CDWs.

We have confirmed the observed nesting by calculations of autocorrelation $R(\mathbf{q}) = \int_{\Omega} I_{\mathrm{F}}(\mathbf{k})I_{\mathrm{F}}(\mathbf{k} + \mathbf{q})d^2\mathbf{k}$ of the (regularized) experimental FS map $I_{\mathrm{F}}(\mathbf{k})$ throughout the BZ cut Ω [15]. The $R(\mathbf{q})$ map in Fig. 3(d) shows a gross arclike peak identifying the nesting vector. As $R(\mathbf{q})$ is less sensitive to sliding of the bands in the $k_{\perp}$ direction, the

peak is elongated in $q_{\perp}$. In principle, the $R(\mathbf{q})$ structures are only connected with $\mathrm{Im}\chi_{\mathbf{q}}$ and might be distorted when carrying them over to $\mathrm{Re}\chi_{\mathbf{q}}$ to define $\mathbf{q}$ of the CDW instability [13]. Despite these potential complications, the experimental $R(\mathbf{q})$ closely matches the actual 3D CDWs: The $R(\mathbf{q})$ peak is centered at $q_{\parallel} \sim 0.52$ Å^{-1} and in the $q_{\perp}$ direction extends from ~ 0.3 to 0.5 Å^{-1}. An energy gain under commensuration of the CDW [12] slightly shifts the system along the $R(\mathbf{q})$ arc to the nearest commensurate $\mathbf{q}$ which are the actual $q_{\parallel}^{\mathrm{CDW}} \sim 0.54$ Å^{-1} and $q_{\perp}^{\mathrm{CDW}} \sim 0.34$ Å^{-1}. The formation of 3D CDWs in VSe$_2$ follows therefore the FS nesting scenario, with their 3D character resulting from the 3D warping of the FS.

We note that formation of 3D CDWs is a rare phenomenon observed, to the best of our knowledge, only for two other TMDCs, TaS$_2$ and TiSe$_2$ [10,31]. Our SX-ARPES results remain so far unique to detail the FS of VSe$_2$, because alternative experimental methods based on quantum oscillations (like the de Haas—van Alphen effect) require large crystals of high purity hardly available for TMDCs. Our picture of the 3D CDWs electronic structure origin calls for a complementary study on the phononic side to identify the corresponding soft phonon mode. While Raman scattering on VSe$_2$ delivers information [28] on phonons only in the Γ point, inelastic x-ray scattering [27] is capable of probing any region of $\mathbf{q}$ space.

Summary.—SX-ARPES benefits from sharp definition of $k_{\perp}$ allowing precise navigation in 3D $\mathbf{k}$ space. Essential for the SX-ARPES experiment is advanced photon flux performance of the synchrotron instrumentation. We have applied SX-ARPES to VSe$_2$ as a paradigm TMDC. The SX-ARPES images of its basic electronic structure characteristics, 3D band structure and FS, demonstrate unprecedented clarity by virtue of free-electron final states, their
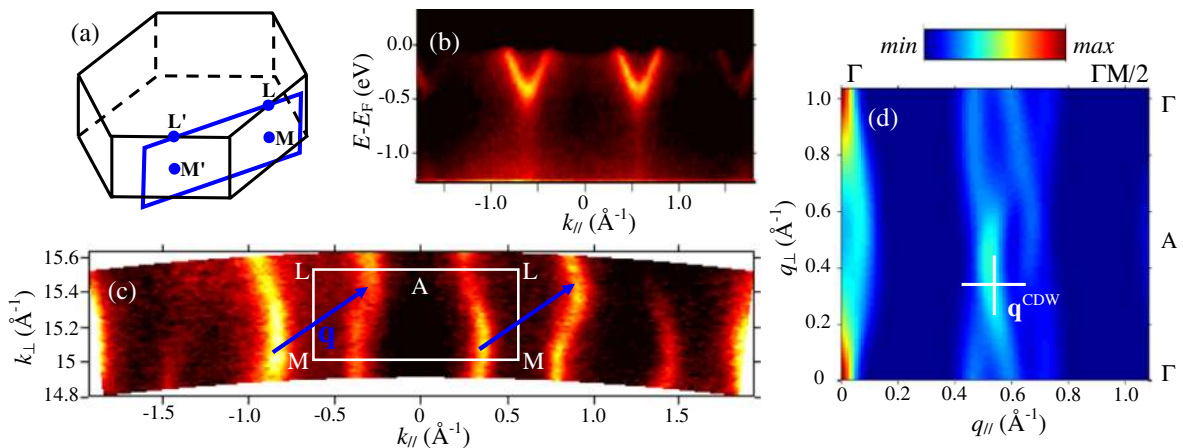

FIG. 3 (color online).   3D warping of the FS in the nesting region as the 3D CDWs precursor. (a) $MLL'M'$ plane of the BZ going through the nesting region; (b) experimental $I(E, k_{\parallel})$ image along the MM' line ($h\nu = 890$ eV); (c) experimental out-of-plane FS cut in the $MLL'M'$ plane ($h\nu = 880$ to 960 eV) normalized similar to Fig. 1(c). The $k_{\perp}$ dispersions are asymmetric due to the threefold symmetry of the BZ interior. 3D warping of the FS contours results in nesting with the indicated $\mathbf{q}$ close to $\mathbf{q}^{\mathrm{CDW}}$ of the 3D CDWs; (d) corresponding $R(\mathbf{q})$ autocorrelation map showing an arclike maximum near $\mathbf{q}^{\mathrm{CDW}}$.

small $\Delta k_\perp$ broadening and smooth photoemission matrix elements. Investigation of the FS nesting properties supported by autocorrelation analysis has shown that its $k_\perp$ warping forms pronounced 3D nesting to act as the precursor for the exotic 3D CDWs. In a broader perspective, our results unfold the immense potential of SX-ARPES to explore the electron realm in 3D crystalline solids.

*Corresponding author. vladimir.strocov@psi.ch.

[1] S. Hüfner, *Photoelectron Spectroscopy: Principles and Applications* (Springer, New York, 1996).

[2] V. N. Strocov, H. I. Starnberg, P. O. Nilsson, and H. E. Brauer, Phys. Rev. Lett. **79**, 467 (1997); V. N. Strocov, H. I. Starnberg, P. O. Nilsson, H. E. Brauer, and L. J. Holleboom, J. Phys. Condens. Matter **10**, 5749 (1998).

[3] V. N. Strocov, E. E. Krasovskii, W. Schattke, N. Barrett, H. Berger, D. Schrupp, and R. Claessen, Phys. Rev. B **74**, 195125 (2006).

[4] V. N. Strocov, J. Electron Spectrosc. Relat. Phenom. **130**, 65 (2003).

[5] S. Suga et al., Phys. Rev. B **70**, 155106 (2004).

[6] M. Mulazzi et al., Phys. Rev. B **82**, 075130 (2010).

[7] A. Sekiyama et al., Phys. Rev. B **70**, 060506(R) (2004).

[8] C. J. Powell, A. Jablonskib, I. S. Tilininc, S. Tanumad, and D. R. Penne, J. Electron Spectrosc. Relat. Phenom. **98–99**, 1 (1999).

[9] V. N. Strocov et al., J. Synchrotron Radiat. **17**, 631 (2010).

[10] A. M. Woolley and G. Wexler, J. Phys. C **10**, 2601 (1977).

[11] H. I. Starnberg, H. E. Brauer, L. J. Holleboom, and H. P. Hughes, Phys. Rev. Lett. **70**, 3111 (1993).

[12] G. Gruener, *Density Waves in Solids* (Addison-Wesley, Reading, MA, 1994).

[13] M. D. Johannes and I. I. Mazin, Phys. Rev. B **77**, 165135 (2008).

[14] S. K. Chan and V. Heine, J. Phys. F **3**, 795 (1973).

[15] D. S. Inosov, V. B. Zabolotnyy, D. V. Evtushinsky, A. A. Kordyuk, B. Büchner, R. Follath, H. Berger, and S. V. Borisenko, New J. Phys. **10**, 125027 (2008).

[16] D. J. Eaglesham, R. L. Withers, and D. M. Bird, J. Phys. C **19**, 359 (1986).

[17] See Supplemental Material at http://link.aps.org/supplemental/10.1103/PhysRevLett.109.086401 for the experimental geometry.

[18] P. Blaha, and J. Luitz et al., *WIEN2k, An Augmented Plane Wave Plus Local Orbitals Program for Calculating Crystal Properties* (Vienna University of Technology, Austria, 2001).

[19] F. Venturini, J. Minár, J. Braun, H. Ebert, and N. B. Brookes, Phys. Rev. B **77**, 045126 (2008).

[20] A. X. Gray et al., Nature Mater. **10**, 759 (2011).

[21] J. J. Yeh and I. Lindau, At. Data Nucl. Data Tables **32**, 1 (1985) (Web version available at http://ulisse.elettra.trieste.it/services/elements/WebElements.html).

[22] A. Önsten, M. Månsson, T. Claesson, T. Muro, T. Matsushita, T. Nakamura, T. Kinoshita, U. O. Karlsson, and O. Tjernberg, Phys. Rev. B **76**, 115127 (2007).

[23] K. Terashima, T. Sato, H. Komatsu, and T. Takahashi, Phys. Rev. B **68**, 155108 (2003).

[24] L. Plucinski, J. Minár, B. C. Sell, J. Braun, H. Ebert, C. M. Schneider, and C. S. Fadley, Phys. Rev. B **78**, 035108 (2008).

[25] G. V. Kamarchuk, A. V. Khotkevich, V. M. Bagatsky, V. G. Ivanov, P. Molinié, A. Leblanc, and E. Faulques, Phys. Rev. B **63**, 073107 (2001).

[26] J. Voit, L. Perfetti, F. Zwick, H. Berger, G. Margaritondo, G. Grüner, H. Höchst, and M. Grioni, Science **290**, 501 (2000).

[27] F. Weber, S. Rosenkranz, J.-P. Castellan, R. Osborn, R. Hott, R. Heid, K.-P. Bohnen, T. Egami, A. H. Said, and D. Reznik, Phys. Rev. Lett. **107**, 107403 (2011).

[28] S. Sugai, Phys. Status Solidi B **129**, 13 (1985).

[29] H. P. Hughes, C. Webb, and P. M. Williams, J. Phys. C **13**, 1125 (1980).

[30] T. Sato, K. Terashima, S. Souma, H. Matsui, T. Takahashi, H. Yang, S. Wang, H. Ding, N. Maeda, and K. Hayashi, J. Phys. Soc. Jpn. **73**, 3331 (2004).

[31] C. Monney et al., New J. Phys. **12**, 125019 (2010).